

# Charge Compensation Mechanisms in Ni-Rich NMC Cathodes

Jesus Díaz-Sánchez,\* Ingeborg S. Ellingsen, Elena Salagre, Jesús Sánchez-Prieto, Noelia Maldonado, Arturo Galindo, Carmen Morant, Enrique Vasco, Gastón García, Daniel Rettenwander, Juan Rubio-Zuazo, Enrique G. Michel, and Celia Polop\*

Understanding charge compensation mechanisms in nickel-rich lithium nickel–manganese–cobalt alloy oxide (NMC) cathodes is crucial for optimizing their electrochemical performance. This study employs complementary spectroscopic techniques with varying probing depths, including X-ray absorption near-edge structure spectroscopy, hard X-ray photoemission spectroscopy, X-ray photoelectron spectroscopy, and ion beam analysis, to investigate the correlation between transition metal oxidation states and Li depth profile in NMC811. This approach reveals different charge compensation mechanisms depending on the local Li content, which exhibits near-surface gradients. The results show that Ni oxidation is the main charge compensation mechanism for moderate delithiations at a Li stoichiometry  $x > 0.35$ .

When the Li content drops below the threshold  $x = 0.3$ , which occurs near the surface for high state of charge (SOC), compensation by Ni/Li mixing prevails. Meanwhile, the Li-depleted surface (with  $x \ll 0.3$ ) shows evidence of transformation into electrochemically inactive Li-free cubic phases. The voltage window used to cycle the NMC811 prevents the bulk Li content from falling below  $x = 0.35$ , so the different charge compensation mechanisms coexist for high SOCs, allowing to compare between their kinetics. This study contributes to a comprehensive understanding of the electrochemical behavior of nickel-rich NMCs, aiding the development of high-energy Li-ion batteries with improved stability.

## 1. Introduction

The global transition toward renewable energy and the rising popularity of electric vehicles (EVs) have significantly increased the demand for advanced energy storage solutions, especially lithium-ion batteries (LIBs).<sup>[1,2]</sup> Among the various components

of the LIBs, the cathode plays a pivotal role in determining the energy density and overall electrochemical performance of the cells. For decades, single transition metal (TM) cathode materials have been widely used in LIBs. Lithium cobalt oxide LiCoO<sub>2</sub> (LCO) was the first ever Li-based cathode to be commercialized, initially favored due to its high theoretical capacity and cyclability. But the

J. Díaz-Sánchez, E. Salagre, E. G. Michel, C. Polop

Department of Condensed Matter Physics

Autonomous University of Madrid (UAM)

28049 Madrid, Spain

E-mail: jesus.diazs@uam.es

celia.polop@uam.es

J. Díaz-Sánchez, C. Morant, E. G. Michel, C. Polop

"Nicolás Cabrera" University Institute of Materials Science (INC)

Autonomous University of Madrid (UAM)

28049 Madrid, Spain

I. S. Ellingsen, D. Rettenwander

Department of material science and engineering

Norwegian University of Science and Technology (NTNU)

7034 Trondheim, Norway

J. Sánchez-Prieto,<sup>[+]</sup> N. Maldonado, G. García

Centre for Micro Analysis of Materials (CMAM)

Autonomous University of Madrid (UAM)

28049 Madrid, Spain

A. Galindo, E. Vasco

Material Science Institute of Madrid (ICMM)

Superior Council of Scientific Investigation (CSIC)

Spanish National Research Council (CSIC)

28049 Madrid, Spain

C. Morant

Department of Applied Physics

Autonomous University of Madrid (UAM)

28049 Madrid, Spain

D. Rettenwander

Christian Doppler Laboratory for Solid-State Batteries

Norwegian University of Science and Technology (NTNU)

7034 Trondheim, Norway

J. Rubio-Zuazo

BM25-Spline

European Synchrotron Radiation Facility (ESRF)

38000 Grenoble, France

E. G. Michel, C. Polop

Condensed Matter Physics Center (IFIMAC)

Autonomous University of Madrid (UAM)

28049 Madrid, Spain

<sup>[+]</sup>Present address: Institute for the structure of Matter (IEM) Superior Council of Scientific Investigation (CSIC), 28049 Madrid, Spain

 Supporting information for this article is available on the WWW under <https://doi.org/10.1002/batt.202500167>

 © 2025 The Author(s). *Batteries & Supercaps* published by Wiley-VCH GmbH. This is an open access article under the terms of the Creative Commons Attribution License, which permits use, distribution and reproduction in any medium, provided the original work is properly cited.

practical limitations to exploit this capacity, together with thermal instabilities and a high cost, led to the exploration of alternatives. Lithium nickel oxide  $\text{LiNiO}_2$  (LNO) was introduced as a potential replacement due to its higher practical capacity,<sup>[3]</sup> but the challenges related to charge compensation by Ni/Li cations mixing lead to a poor cyclability which prevents its leap into the industry.<sup>[4]</sup> On the other hand, lithium manganese oxide  $\text{LiMnO}_2$  (LMO) demonstrated structural stability<sup>[5]</sup> but suffered from rapid capacity fading due to Jahn-Teller distortions caused by high local concentrations of  $\text{Mn}^{3+}$ .<sup>[6]</sup> To overcome these limitations, advanced cathodes based on multi-TM alloys have been developed. Among them, the NMC family of compounds ( $\text{Li}_{x}\text{Ni}_y\text{Mn}_z\text{Co}_{1-y-z}\text{O}_2$ ) stands out,<sup>[7-9]</sup> offering improved electrochemical properties, higher practicable capacities, better cyclability and rate performance, and enhanced safety. Thus, in general, while single TM cathodes undergo a phase transformation under deep delithiation conditions from layered hexagonal to a cubic phase, NMC compounds have been regarded as stable against the phase transformation. This enables access to a wider reversible delithiation range down to a Li stoichiometry of  $x = 0.35$  compared to the typical  $x = 0.5$  of single-TM cathodes ( $x$  refers to the Li stoichiometry in the NMC compound, namely,  $\text{Li}_x\text{Ni}_y\text{Mn}_z\text{Co}_{1-y-z}\text{O}_2$ ). The composition of NMC compounds significantly influences their properties. While higher Mn and Co contents enhance structural stability and cyclability respectively, they do so at the expense of total capacity. Conversely, increasing Ni concentration significantly improves capacity but has the potential to compromise cyclability.<sup>[7]</sup> Nickel-rich NMC cathodes have thus gained prominence, particularly for high-energy applications,<sup>[8]</sup> and these are now used in EVs by major manufacturers like Tesla, BMW, Mercedes Benz-Daimler, and Nissan.<sup>[1]</sup> Among these,  $\text{LiNi}_{0.8}\text{Mn}_{0.1}\text{Co}_{0.1}\text{O}_2$  (NMC811) stands out due to its high energy density and specific capacity.<sup>[9]</sup> However, the high Ni content in NMC811 reintroduces Ni/Li cation mixing as a major charge compensation mechanism under deep delithiation conditions. Understanding how the coexistence of multiple charge compensation pathways affects the electrochemical behavior of NMC cathodes is of great scientific and engineering interest. This understanding is essential for optimizing the NMC811 performance and longevity in advanced battery applications.

In single TM cathode materials, charge compensation during delithiation within the standard range of operation occurs mainly through the TM oxidation. Deep delithiation at higher overvoltage giving rise to Li concentrations  $<50\%$  induces irreversible structural transitions from the layered hexagonal phase (S.G. R-3m) toward cubic spinel (S.G. Fd-3 m). A subsequent delithiation produces a nonelectrochemical rock salt cubic phase (S.G. Fm-3m) characterized by cationic disorder. The NMC compounds also undergo irreversible structural changes of the same nature, transitioning from a layered to spinel and eventually to a rock salt phase.<sup>[10,11]</sup> The phase transitions have been extensively studied, as the lower Li diffusion, higher resistivity, and irreversibility of the spinel and rock salt phases prevent the cathode to recover the stoichiometric Li concentration during the discharge, and reduce significantly the capacity of the cell, especially when working at overvoltage higher than 4.5 V (from loses of 0.02% of capacity per

cycle at 4.3 V to more than 1.5% loses per cycle at 4.7 V).<sup>[12,13]</sup> Ni-rich NMCs (e.g., NMC811) promise better energy density because they can tolerate deeper delithiation regimes before phase transitions significantly impact their capacities.<sup>[13]</sup> Beyond the charge compensation by oxidation, Ni-rich NMC introduces Ni/Li cation mixing as another charge compensation mechanism.<sup>[14,15]</sup> This phenomenon was first identified in  $\text{LiNiO}_2$ , precursor of Ni-rich NMC cathodes. It was observed that  $\text{LiNiO}_2$  tends to crystallize with excess Ni, adopting a nonstoichiometric composition of  $[\text{Li}_{1-z}\text{Ni}_z^{2+}]^{\text{Li layer}} [\text{Ni}_{1-z}^{3+}\text{Ni}_z^{2+}]^{\text{TM layer}} \text{O}_2$ , where  $\text{Ni}^{2+}$  cations occupy positions in the Li slab due to their similar ionic radii (0.69 Å for  $\text{Ni}^{2+}$  versus 0.76 Å for  $\text{Li}^{+}$ ). This occupation leads to the partial reduction of  $\text{Ni}^{3+}$  in the TM layer to maintain charge neutrality. Measurements of the Ni L-edge confirmed that the excess Ni was in the  $\text{Ni}^{2+}$  state,<sup>[4]</sup> as evidenced by the increasing similarity between the Ni L-edge X-ray absorption near-edge structure spectroscopy (XANES) spectra of  $\text{LiNiO}_2$  and  $\text{NiO}$  with growing Li deficiency. Facilitated by the presence of oxygen vacancies,  $\text{Ni}^{3+/4+}$  cations migrate from the transition metal octahedral (TM-O<sub>6</sub>) layer to Li-depleted regions, being reduced to  $\text{Ni}^{2+}$ . Direct observation by scanning transmission electron microscopy (STEM) and density functional theory calculations (DFT) allows identification of three different Ni cation migration pathways: single-atom migration to Li vacancies, Ni–O co-migration, and sequential oxygen-assisted migration.<sup>[16-18]</sup> Among these modalities, Ni–O co-migration has the lowest formation energy, implying a preference over the single Ni-ion migration.<sup>[16]</sup> DFT calculations indicate that the energy barrier for cation mixing decreases with decreasing Li concentration and can become spontaneous at intermediate state of charge (SOC) levels. While Li/Ni mixing does not reduce the accessible capacity directly, it can damage the electrochemical performance by inducing voltage decay in the surface layers. This effect is associated with the presence of shorter Ni–O bonds in NiO<sub>6</sub> octahedra located within the Li layer,<sup>[17]</sup> which hinders Li extraction in the Li/Ni mixing regions. As a result, the battery performance at high SOCs could be negatively affected.

Understanding the evolution of the oxidation states of TMs and evaluating the charge compensation mechanisms in NMC cathodes are essential to improve the performance of batteries based on NMC compounds. XANES has been widely used for this purpose. XANES-based studies show that in NMC111,  $\text{Mn}^{4+}$  and  $\text{Co}^{3+}$  remain stable during charging, while  $\text{Ni}^{3+}$  oxidizes progressively to  $\text{Ni}^{4+}$  to compensate for delithiation.<sup>[4]</sup> Similar findings in Ni-rich NMC cathodes confirm that Ni oxidation remains the primary charge compensation process, while the oxidation states of Co and Mn remain stable.<sup>[19-22]</sup> However, since XANES is a bulk-sensitive technique with  $\approx 1 \mu\text{m}$  probing depth, this technique provides bulk-averaged oxidation states without depth resolution. To overcome this limitation, X-ray photoelectron spectroscopy (XPS) is used for surface oxidation state analysis (with a  $\approx 1 \text{ nm}$  probing depth).<sup>[14,23-26]</sup> However, the extreme surface sensitivity of XPS limits its ability to distinguish massive processes happening beyond the surface. Hard X-ray photoemission spectroscopy (HAXPES) bridges this gap between surface and bulk sensitivity by probing deeper

( $\approx 10$  nm) while still resolving individual oxidation states, making it a valuable complement to XPS and XANES. Additionally, ion beam analysis (IBA) techniques, comprising Rutherford backscattering spectroscopy (RBS) and nuclear reaction analysis (NRA), precisely quantify Li distribution profiles at  $\approx 10 \mu\text{m}$  probing depth in Li-cathodes<sup>[27–29]</sup> allowing to directly link the evolution of the TM oxidation states with dissimilar charge compensation mechanisms at different depths during cathode cycling.

This study employs XANES, HAXPES, and XPS, along with Li depth profiles for different SOCs measured by IBA, to investigate the evolution of TM oxidation states at various depths. This approach enables a comprehensive understanding of the charge compensation mechanisms operating in Ni-rich NMC cathodes. By examining the interplay between Ni oxidation, Ni/Li mixing, and phase transitions at different depths and SOCs, we aim to develop a thorough understanding of the response of NMC811 cathodes to delithiation, which will contribute to the advancement of high-performance cathodes for next-generation LIBs.

## 2. Experimental Section

### 2.1. Cathode Preparation and Electrochemical Cycling

Cathode tapes were prepared by mixing  $\text{LiNi}_{0.8}\text{Co}_{0.1}\text{Mn}_{0.1}\text{O}_2$  (Targray, SNMC03008) powder, Carbon black (Imerys, C-NERGY Super C65), and polyvinylidene fluoride (PVDF) (Arkema, Kynar

HSV 900) in an 85:10:5 weight ratio. The mixture was combined with 1-methyl-2-pyrrolidinone (NMP) (Alfa Aesar, W06H804) at a 1:2 dry materials-to-NMP weight ratio and processed in a Retsch Mixer MM400 shaker mill for 30 min at 25 Hz using  $\text{ZrO}_2$ -lined jars. The resulting slurry was tape-cast onto Al foil with a 300  $\mu\text{m}$  gap doctor blade, dried at 80 °C for 20 min, and vacuum-dried at 120 °C overnight. The resulting cast was calendared, cut into circular 10 mm diameter discs, and transferred into an Ar glovebox ( $\text{H}_2\text{O} < 0.1 \text{ ppm}$ ,  $\text{O}_2 < 0.1 \text{ ppm}$ ).

For coin cell assembly, electrodes were weighed and assembled into 2016 encapsulated half-cells with trilayer PP/PE/PP separators (Celgard 2325) wetted in 40  $\mu\text{L}$  of a 1.0 M  $\text{LiPF}_6$  / Li metal counter electrodes (14 mm diameter), and 0.3 mm stainless steel spacers. Galvanostatic charge–discharge cycling was performed between 2.8 and 4.2 V (versus Li/Li $^+$ ) with exception of the first cycle which was completed between 2.8 and 4.3 V. The two initial cycles were done at C/10 and six remaining cycles at C/2 (except the sample at SOC = 0 %, which was only cycled once at C/10). Cells were charged to different SOCs by setting the cut-off voltage corresponding to a defined fraction of the capacity measured in the previous cycle at 4.2 V. The voltage was selected such that charging was interrupted once the targeted capacity fraction had been delivered. Figure 1a shows the charge–discharge profile of the cell left at SOC = 75 %. The disassembly of the cells was carried out in an Ar-filled glovebox. The charged NMC cathodes were extracted, rinsed with battery-grade DMC (Sigma–Aldrich), and vacuum-dried for at least 2 h.

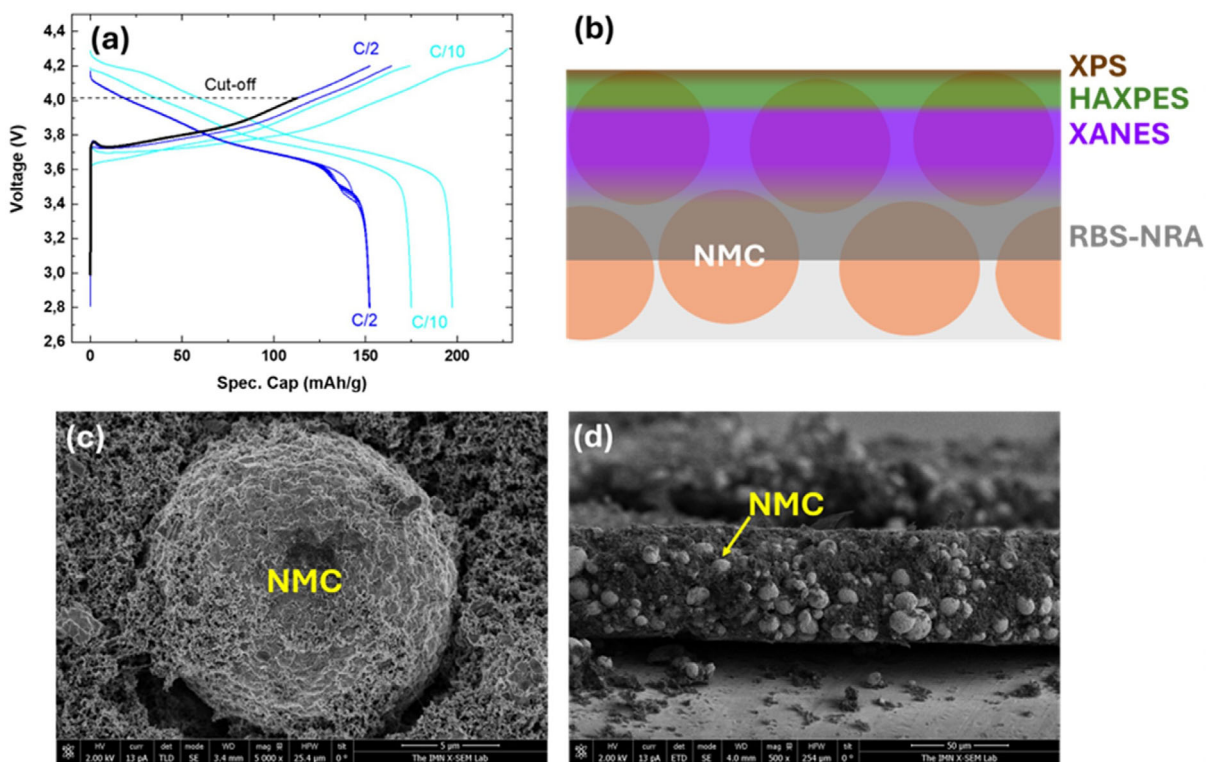


**Figure 1.** a) Specific capacity plot from C/10- (light blue) and C/2-rate (dark blue) cycles in SOC = 75% for NM811 cathode. Thicker black line marks the final cycle up to the cut-off voltage. b) Not-scale scheme of the depth sensitivity of the different chemical state sensitive spectroscopies used in this work. c) and d) SEM images of an NMC811 secondary particle (top view) and the pristine cathode (cross-section), respectively.

## 2.2. Cathode Characterization

Once extracted from the disassembled cells, the NMC cathodes at different SOCs were studied in terms of microstructure by scanning electron microscopy (SEM), composition and Li content by IBA, and TM oxidation states by X-ray spectroscopy techniques (XANES, HAXPES, and XPS).

The morphology of the cathodes was studied by SEM using an FEI Verios 460 L system operating at 2 kV, which integrated a Quantax energy-dispersive X-ray spectroscopy (EDS) analyzer (by Thermo Fisher Scientific).

The NMC cathodes were characterized using IBA at the Center for Microanalysis of Materials (CMAM).<sup>[30]</sup> IBA comprised simultaneous measurements by NRA and RBS, both using a 3 MeV proton beam at a high-current coaxial tandem accelerator with a terminal potential of 5 MV. These techniques provided complementary information about the atomic composition of the samples with depth resolution. Specifically, NRA was sensitive to light-weight elements, such as Li and F due to nuclear reactions  $^7\text{Li}(\text{p},\alpha_0)^4\text{He}$  and  $^{19}\text{F}(\text{p},\alpha_0)^{16}\text{O}$  respectively. F originated from the NMC/binder and NMC/electrolyte interfaces. In contrast, RBS was effective for detecting heavier elements, including TMs, O, and C through elastic collision with protons. In our setup, both the particles resulting from nuclear reactions and those backscattered were detected simultaneously in two surface barrier detectors (with energy resolution of 12 and 18 keV), which are placed at  $\Theta = 170^\circ$  and  $150^\circ$  from the beam direction in ion-beam modification (IBM) geometry, respectively. The resulting spectra were analyzed using SIMNRA 7.03 code,<sup>[31]</sup> employing collisional cross-sections reported by Paneta et al.<sup>[32]</sup> The combination of both techniques offered a comprehensive analysis of the composition depth profiles of the NMC cathodes, with a depth probing up to 12  $\mu\text{m}$  with 80 nm sensitivity.

HAXPES and XANES measurements were carried out at the BM25-Spline beamline of the ESRF using synchrotron X-ray radiation in the 5–45 keV energy range with high photon flux ( $\approx 10^{13}$  photons/s). The HAXPES setup included a 2-pole wiggler at the D25 port coupled to a Si(111) double-crystal monochromator for precise energy selection and a CSA300-HV cylindrical sector analyzer equipped with a preretarding lens system to optimize energy resolution for electron kinetic energies up to 15 keV.<sup>[33–35]</sup> HAXPES measurements at  $h\nu = 13$  keV were used to analyze the oxidation states of Ni, Mn, and Co at depths beyond the reach of conventional XPS, focusing on their respective 1s peaks due to optimized photoemission cross-sections. While the Ni 2p peak was also successfully measured, the corresponding Mn and Co 2p signals exhibited insufficient intensity for reliable detection without significantly longer acquisition times. Additional measurements included the C 1s and O 1s peaks, as well as a wide-range overview scan covering binding energies below 1 keV. On the other hand, the XANES measurements were performed in fluorescence mode at RT and normal pressure using a Hitachi Vortex Si drift detector with 2 mm chip thickness for low and high energy detection coupled to XIA Falcon X electronics. A low angle of incidence was used to avoid self-absorption. The data were plotted and analyzed using Athena and Hephaestus

codes.<sup>[36]</sup> Fluorescence spectroscopy composition data obtained at  $h\nu = 13$  keV were fitted and analyzed using PyMca 5.1.3.<sup>[37]</sup> The results are provided in section S1, Supporting Information.

XPS experiments were performed at a laboratory using an X-ray source from a Mg anode to measure Ni 2p, Ni 3p, Co 3p, Li 1s, Mn 3p, C 1s, O 1s peaks, along with an overall survey spectrum for binding energy (BE) below 1 keV. Similarly, an Al anode was used to measure Co 2p, F 1s, and Mn 2p core levels under similar conditions. The photoelectrons were detected with a Phoibos 150 hemispherical analyzer. The spectra were plotted, analyzed using Igor Pro 6.3.<sup>[38]</sup> The core-level line shapes were analyzed using a Shirley background and asymmetric singlet pseudo-Voigt functions. The fitting was performed with the XPTS extension for Igor Pro, which enables energy-dependent variation of peak width to accurately capture the natural asymmetry characteristic of many photoemission signals.<sup>[39]</sup>

As mentioned in the introduction, the X-ray spectroscopy techniques employed in this study exhibited varying depth sensitivities (XANES  $\approx 1 \mu\text{m}$ , HAXPES  $\approx 10 \text{ nm}$ , and XPS  $\approx 1 \text{ nm}$ , as illustrated in Figure 1b). This diversity allowed us to explore the evolution of depth profiles for both Li concentration and TM oxidation states with rising battery SOC. The correlation between these evolutions offers insights into the mechanisms of charge compensation during battery operation.

## 3. Results and Discussion

Figure 1c,d shows SEM images of a pristine NMC particle and cross-section of a pristine NMC811 cathode respectively, pointing to a NMC particle mean diameter of 5–10  $\mu\text{m}$  and a mean cathode thickness of around 50  $\mu\text{m}$ .

Figure 2a shows the RBS and NRA spectra (data points) for the pristine sample along with their simulations (curves) by SIMNRA. The kinetic energy of the protons (3 MeV  $\text{H}^+$ ) determines the crossover between the elastic contribution of RBS (lower energy region on the spectra) and the particles resulting from nuclear reactions (higher energy region). The heavier species (Ni, Co, and Mn) exhibit RBS bands extending from 2.8 MeV on the surface to lower energies within the cathode bulk, while the RBS bands of lighter elements such as F, O, N and C appear on the surface at lower energies of 2.45, 2.36, 2.3, and 2.2 MeV, respectively. On the other hand, for energies greater than 3 MeV, the  $^7\text{Li}$  and  $^{19}\text{F}$  NRA bands extend up to energies of 7.7 and 7.9 MeV respectively, resulting from the characteristic energy-mass balances of the nuclear reactions  $^7\text{Li}(\text{p},\alpha_0)^4\text{He}$  and  $^{19}\text{F}(\text{p},\alpha_0)^{16}\text{O}$ . The energy corresponding to the contribution of each element at the surface is indicated with an upward arrow. The high energy of the  $^7\text{Li}$  NRA band allows us to obtain the Li concentration without interference from RBS signals, unlike the 3–4 MeV region, which cannot be simulated due to the presence of pile-up artifacts from the RBS spectra.<sup>[40]</sup> The inset in Figure 2a shows the evolution of the intensity of the  $^7\text{Li}$  NRA band with the battery SOC. As expected, the band intensity decreases significantly as SOC increases, indicating a decrease in Li concentration.

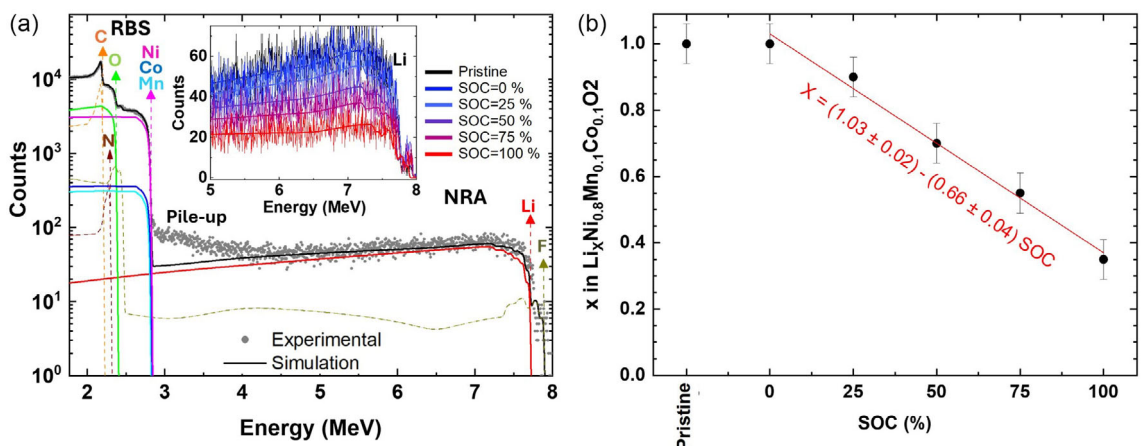


**Figure 2.** a) Fitted RBS/NRA spectra of the pristine sample. Inset shows the drop in the Li NRA band as the battery SOC increases. b) Evolution of the Li concentration measured by NRA with increasing SOC. Red line corresponds to the linear fit of the results.

Simulations of the RBS and NRA spectra for different SOCs allow us to calculate the SOC dependence of the Li stoichiometry ( $x$ ) in the NMC811 compound (namely,  $\text{Li}_{1-x}\text{Ni}_{0.8}\text{Co}_{0.1}\text{Mn}_{0.1}\text{O}_2$ ), as displayed in Figure 2b. Both pristine and 0% SOC-discharged cathodes correspond to Li stoichiometric NMC811 with  $x = 1$ . In contrast, 100% SOC corresponds to  $x = 0.35$ . The simulation shows that delithiation occurs homogeneously across the cathode bulk (see section S2, Supporting Information). Due to the depth resolution of IBA techniques, the surface Li stoichiometry estimated from the results in Figure 2 corresponds to a value averaged over the first 80 nm below the cathode surface. The

SOC dependence of Li stoichiometry in Figure 2b fits reasonably well to a straight line, allowing us to extrapolate the Li content in NMC811 for any battery SOC:  $x(\text{bulk}) = (1.03 \pm 0.02) - (0.66 \pm 0.04) \cdot \text{SOC}$ .

Figure 3 presents the XANES spectra at the K-edges of Ni (Figure 3a), Co (Figure 3b), and Mn (Figure 3c) measured at different SOCs. To aid in feature identification, the second derivative of each spectrum is shown below the corresponding plot. Several characteristic features can be distinguished: (i) the pre-edge peak  $\alpha$ , located at lower photon energies and attributed to the dipole-forbidden  $1s \rightarrow 3d$  electronic transition, appears with nonzero

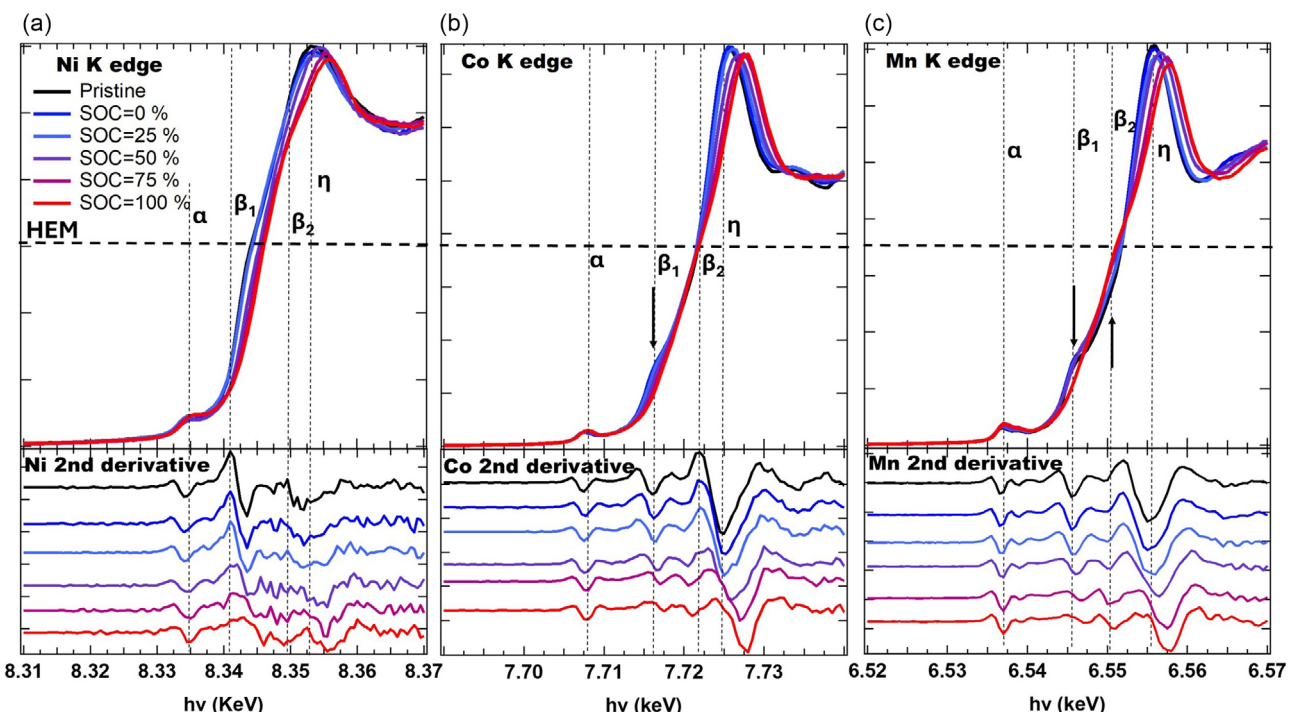


**Figure 3.** a-c) The evolution of the Ni, Co, and Mn K-edges, respectively, with SOC, obtained by XANES. The second derivative of the spectra is shown at the bottom of each graph to help visualize the different features.

intensity due to 3d–4p orbital mixing under quadrupole coupling; (ii) the main peak  $\eta$ , observed at higher photon energies, corresponds to the dipole-allowed  $1s \rightarrow 4p$  transition; (iii) the  $\beta_1$  and  $\beta_2$  peaks arise from the same transition as  $\eta$  but are modified by charge-transfer effects involving O 2p ligand states (shakedown processes), which shift the excitation energy to lower values. The initial oxidation states in the pristine sample were estimated by comparing the edge positions of Ni, Co, and Mn to reference spectra from previous studies.<sup>[20]</sup> The results indicate the presence of Ni<sup>3+</sup>, Co<sup>3+</sup>, and Mn<sup>4+</sup>. However, to maintain charge neutrality given the presence of Mn<sup>4+</sup>, some Ni must be in the Ni<sup>2+</sup> state. Therefore, we infer an average Ni oxidation state of Ni<sup>2.875+</sup> in the pristine material. This is consistent with previous reports on NMC compounds with varying Ni content, where Co and Mn remain as Co<sup>3+</sup> and Mn<sup>4+</sup>, while the Ni oxidation state increases from Ni<sup>2+</sup> in NMC111 to Ni<sup>3+</sup> in Ni-rich compositions.<sup>[19–22,41]</sup> The main peak  $\eta$  corresponds to final-state configurations of  $1s^1\text{s}3d^74p^1$  (Ni<sup>3+</sup>),  $1s^1\text{s}3d^64p^1$  (Co<sup>3+</sup>), and  $1s^1\text{s}3d^34p^1$  (Mn<sup>4+</sup>), while the prepeak  $\alpha$  arises from transitions to  $1s^1\text{s}3d^8$ ,  $1s^1\text{s}3d^7$ , and  $1s^1\text{s}3d^4$ , respectively. Here,  $s$  denotes a hole in the 1s core level.

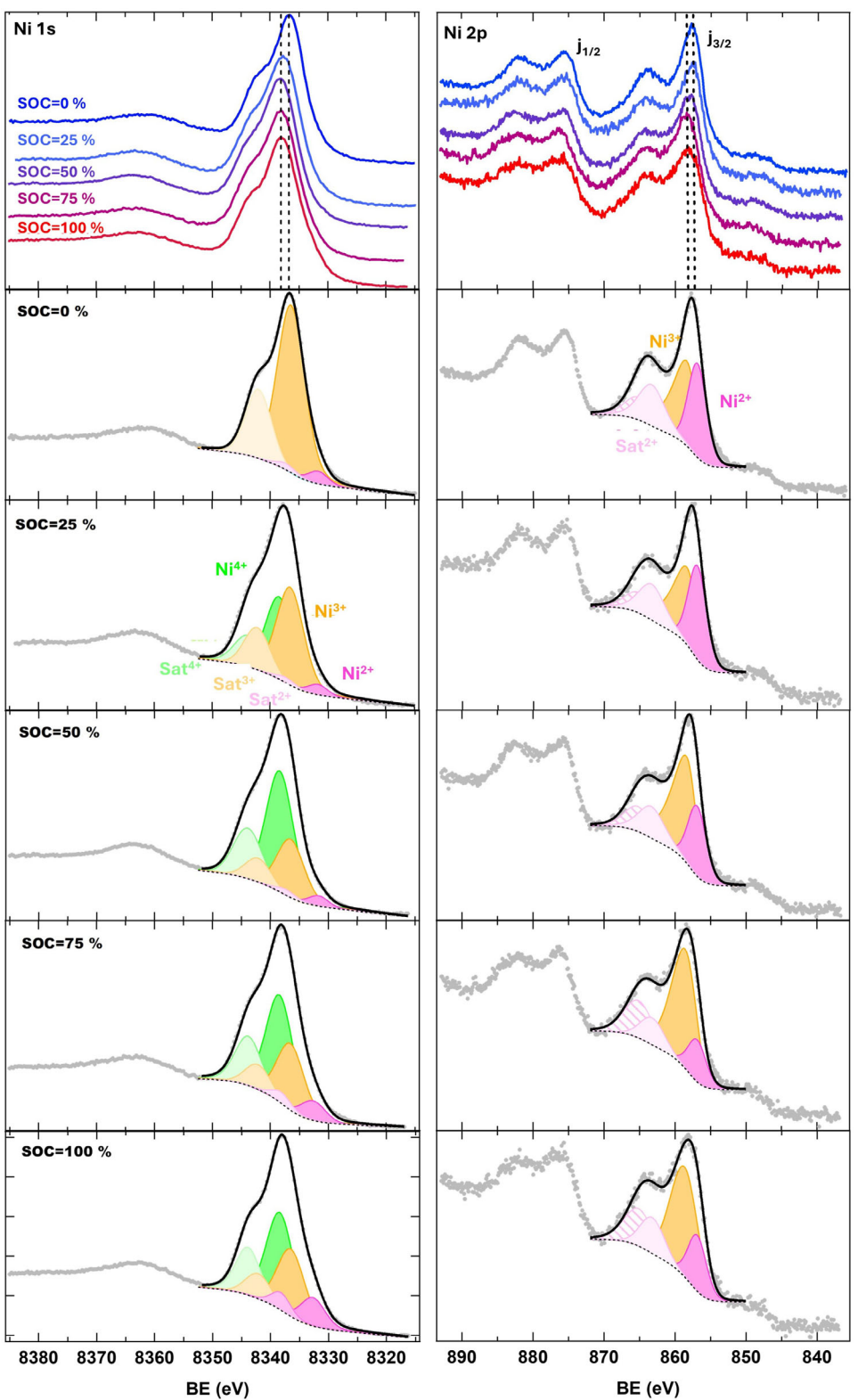
A closer examination of the absorption edge energy—estimated at half the maximum intensity (referred to hereafter as the half edge maximum, or HEM, in Figure 3)—reveals a noticeable shift of the Ni HEM toward higher energies with increasing SOC. In contrast, the HEMs for Mn and Co remain largely unchanged. Apparent downward shifts in the Mn HEM are attributed to variations in the intensity of the  $\beta_1$  and  $\beta_2$  peaks, as confirmed by the second-derivative spectra in Figure 3. The intensity changes observed in the  $\beta_1$  and  $\beta_2$  features for Co and Mn (highlighted with black arrows in Figure 3) are commonly linked to slight alterations in the local metal–oxygen bond lengths during delithiation, which affect 4p orbital hybridization.<sup>[19,20,22]</sup> Further discussion of this effect is provided in section S3, Supporting Information. The energy shift observed in the Ni HEM strongly suggests that Ni is the only redox-active transition metal during battery charging, whereas Mn and Co retain their oxidation states and do not participate in the electrochemical processes. This behavior aligns with previous findings on transition-metal valence states in various NMC materials, including NMC811,<sup>[21]</sup> NMC111,<sup>[19,22]</sup> Ni<sub>0.65</sub>Co<sub>0.25</sub>Mn<sub>0.1</sub>,<sup>[20]</sup> and NMC622.<sup>[41]</sup> By measuring the energy difference between the Ni HEM at a given SOC and that of the pristine state, the Ni oxidation state can be quantitatively estimated.<sup>[42]</sup> Given the penetration depth of XANES ( $\approx 1 \mu\text{m}$ ), these measurements reflect the bulk evolution of transition-metal oxidation states as a function of SOC. The progressive shift of Ni to higher oxidation states upon delithiation supports a charge compensation mechanism dominated by Ni oxidation, as further discussed below.

Figure 4 shows the evolution of HAXPES (left column) and XPS (right column) spectra as a function of SOC. The fitted spectral components corresponding to the main peaks are highlighted in intense colors, while their respective satellites are shown in lighter shades. The deconvolution procedure is explained in detail in section S4, Supporting Information. In the HAXPES spectra (left), the Ni 1s region is shown over the BE range of 8315–8385 eV. At SOC = 0%, the main Ni 1s peak

appears at 8336.6 eV, with a pronounced shoulder 6 eV to the left, attributed to a shake-up satellite.<sup>[43]</sup> A background plasmon feature is also visible at 8362.5 eV. Based on the XANES results, the dominant species at this stage is assigned to Ni<sup>3+</sup> (highlighted in orange). As SOC increases, the main peak shifts to higher BE, reaching 8338.1 eV at SOC = 50%. Simultaneously, the left shoulder becomes less defined, indicating the emergence of a new component at higher BE. The appearance of this component during delithiation, combined with its spectral position, suggests the formation of Ni<sup>4+</sup> (highlighted in green). This interpretation is supported by the concurrent K-edge shift observed in XANES (Figure 3). At SOC > 50%, the main peak shifts slightly back by around 0.3 eV to lower BE, and the left shoulder partially recovers, suggesting a partial reduction of Ni<sup>4+</sup> back to Ni<sup>3+</sup>. Additionally, the peak broadens toward lower BE, indicating the appearance of a third component. Its lower BE suggests it corresponds to Ni<sup>2+</sup> species (highlighted in magenta), consistent with local chemical heterogeneity at high SOCs. The fitting of HAXPES Co 1s and Mn 1s peaks is presented in section S5, Supporting Information, as well as the representation of the HAXPES spectra of C 1s, O 1s, Ni 2p, and an overview for BE < 1000 eV.

The XPS spectra (right column of Figure 4) focus on the Ni 2p region, covering 835–895 eV. The spectra display the characteristic spin-orbit split Ni 2p<sub>3/2</sub> and 2p<sub>1/2</sub> peaks at 857.5 eV and 875 eV, respectively. Both peaks show broad satellite features at 3–5 eV higher BE. The formation of a 2p core hole leads to strong Coulomb repulsion with 3d electrons. This can be partially screened by charge transfer from the O 2p ligand band to the 3d orbital. The resulting final-state configurations are  $2p^5\text{p}3d^8\text{L}$  for Ni<sup>3+</sup> and  $2p^5\text{p}3d^9\text{L}$  for Ni<sup>2+</sup>. Here, p and L denote a hole in the 2p core level and in the ligand band, respectively. In low-spin octahedral Ni<sup>3+</sup>, charge transfer is favored, reducing satellite intensity. In contrast, high-spin Ni<sup>2+</sup> can photoemit without ligand screening, leading to the  $2p^5\text{p}3d^8$  and  $2p^5\text{p}3d^{10}\text{L}^2$  configurations<sup>[44]</sup> and intense satellites, respectively represented with light pink and pink-patterned components in Figure 4. Thus, the presence of prominent satellite peaks is indicative of significant Ni<sup>2+</sup> content, even at SOC = 100%. As SOC increases, the Ni 2p<sub>3/2</sub> peak shifts to higher BE, from 857.6 eV for SOC = 0 % to a maximum of 858.2 eV for SOC = 75%, while the satellites become less defined. This trend suggests an increasing proportion of Ni<sup>3+</sup>, which reduces the energy separation between the main peak and its satellites. At higher SOCs, the main peak shifts slightly back to lower BE. Compared to HAXPES, the XPS peak shift is less pronounced, likely due to its greater surface sensitivity, which results in lower sensitivity to bulk redox changes. XPS peaks of Ni 2p, Ni 3p, Co 3p, Li 1s, Mn 3p, C 1s, O 1s, Co 2p, F 1s, and Mn 2p are presented in section S6, Supporting Information.

Figure 5a shows SOC dependences of the Ni mean oxidation state as measured by XANES (purple), HAXPES (dark green), and XPS (brown). The contribution from the XPS-measured depth has been removed from the HAXPES data in Figure 5a, ensuring that the green line exclusively represents the oxidation state of the subsurface volume (depth  $\approx 10 \text{ nm}$ ). XPS reveals that the Ni oxidation state at the cathode surface is relatively insensitive to battery SOC. This, combined with the fact that the mean



**Figure 4.** (Left column) Ni 1s core-level spectra measured by HAXPES ( $h\nu = 13$  keV) at different SOCs and deconvolution in 3 components corresponding to  $\text{Ni}^{4+}$  (green),  $\text{Ni}^{3+}$  (orange), and  $\text{Ni}^{2+}$  (pink). (Right column) Ni 2p core-level spectra measured by XPS at different SOCs and deconvolution in the  $\text{Ni}^{2+}$  (pink) and  $\text{Ni}^{3+}$  (orange) contributions. Satellites are shown in lighter shades.

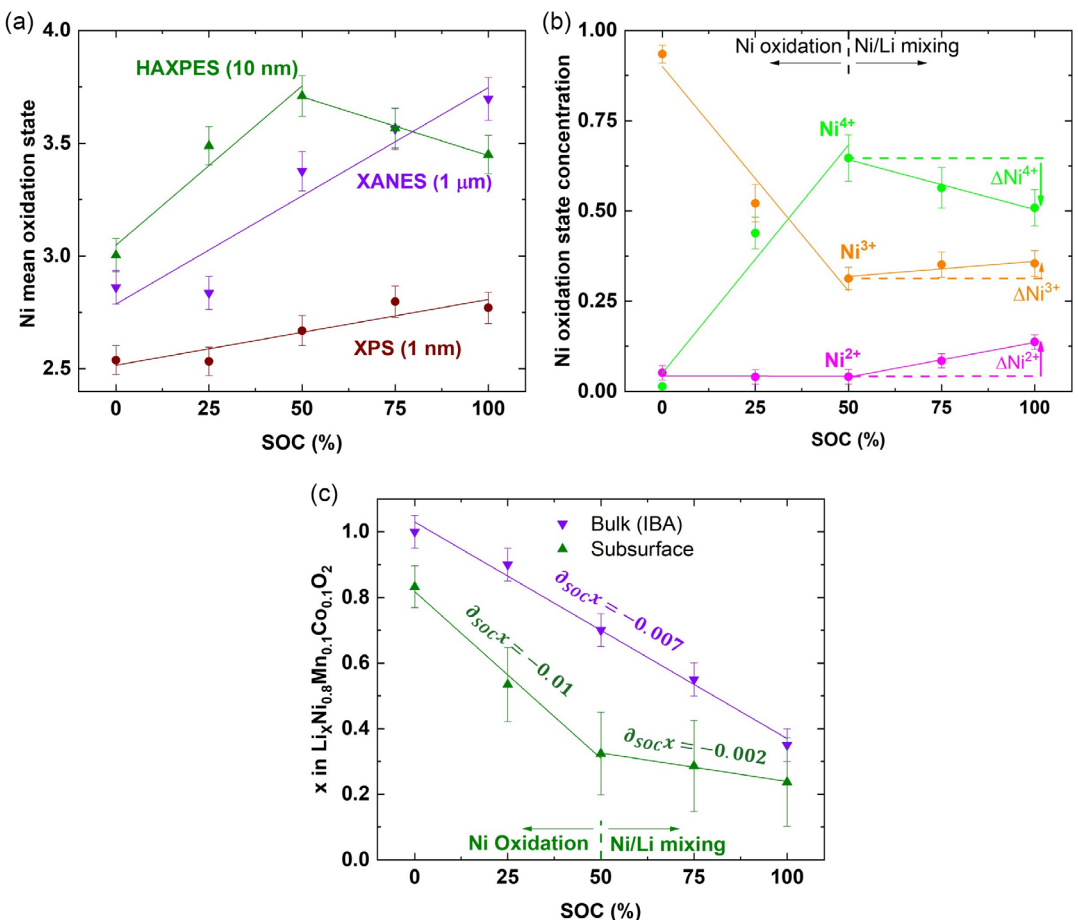
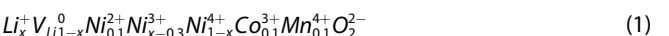


**Figure 5.** a) Evolution of mean Ni oxidation state with battery SOC measured by XANES (purple), HAXPES (dark green), and XPS (brown). HAXPES contribution has been corrected to not include the XPS measured area and therefore be representative of the subsurface region. b) HAXPES contribution of  $\text{Ni}^{4+}$  (green),  $\text{Ni}^{3+}$  (orange), and  $\text{Ni}^{2+}$  (pink) with increasing battery SOC. c) Li concentration measured within volume NMC811 by IBA (violet) and estimated in the subsurface by model interpolation (dark green).

oxidation state varies within the range of 2.5–2.8 (below pristine  $\text{Ni}^{2.875+}$ ), indicates that the cathode surface is depleted in Li and rich in low-coordination Ni oxide phases (mostly  $\text{Ni}_3\text{O}_4$  and  $\text{NiO}$ ). The XANES results suggest that charging of the NMC cathode leads to progressive bulk oxidation of  $\text{Ni}^{3+}$  into  $\text{Ni}^{4+}$ . A more complex behavior is observed by the Ni oxidation state within the subsurface layer inspected by HAXPES. The oxidation state rises quickly as the battery SOC increases to 50% and then drops at higher SOCs. To understand this behavior, Figure 5b displays the evolution of the  $\text{Ni}^{2+}$ ,  $\text{Ni}^{3+}$ , and  $\text{Ni}^{4+}$  contributions to the HAXPES Ni 1s peak (deconvoluted in Figure 4, left column). The initial increase in Ni mean oxidation state results from the oxidation of  $\text{Ni}^{3+}$  to  $\text{Ni}^{4+}$ , with complementary trends in their populations (i.e., the  $\text{Ni}^{3+}$  population drops at the same rate as the  $\text{Ni}^{4+}$  population rises), while the  $\text{Ni}^{2+}$  population remains negligible. Beyond SOC = 50%, the  $\text{Ni}^{2+}$  population increases, the  $\text{Ni}^{3+}$  population also does so although more slightly, while the  $\text{Ni}^{4+}$  population decreases. This results in a decrease in the mean Ni oxidation state beyond SOC > 50%, as shown in Figure 5a.

During the first stages of battery charging, the cathode delithiation can be compensated by the oxidation of the TMs. In the

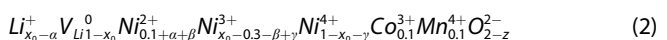
case of NMC811, our XANES results demonstrate that only Ni oxidizes from  $\text{Ni}^{3+}$  into  $\text{Ni}^{4+}$  in the same proportion as Li vacancies ( $V_L$ ) are created. This ensures that the resulting compound becomes



This is consistent with the results found in Figure 5b for battery SOC  $\leq 50\%$ , namely (i) the  $\text{Ni}^{2+}$  population, which results from compensating the  $\text{Mn}^{4+}$  population, is independent of the Li content; and (ii) the  $\text{Ni}^{3+}$  and  $\text{Ni}^{4+}$  populations exhibit opposite behaviors. While  $\text{Ni}^{3+}$  decreases as the Li content  $x$  drops,  $\text{Ni}^{4+}$  increases as  $1 - x$ . These findings align with previous published works where XANES was used to study the evolution of TM oxidation state in NMC811<sup>[21]</sup> and other Ni-rich NMCs such as NMC622<sup>[41]</sup> and  $\text{Ni}_{0.65}\text{Co}_{0.25}\text{Mn}_{0.1}$ .<sup>[20]</sup> These studies found that Ni oxidation alone was responsible for compensating charge during delithiation, while  $\text{Co}^{3+}$  and  $\text{Mn}^{4+}$  remain electrochemically inactive.

In contrast to TM oxidation compensation, an alternative charge compensation mechanism via the mixing of Li/Ni cations

prior to potential phase transitions is also available for Ni-rich NMC compounds. This mechanism involves the migration of  $Ni^{3+/4+}$  cations to the Li sites occupied by vacancies with their consequent reduction to  $Ni^{2+}$ . This process is accompanied by the reduction of other oxidized species in a proportion similar to the amount of migrated Ni. The compound that results from the Li/Ni cation mixing mechanism in NMC811 becomes



where  $x_0$  is the Li stoichiometry at which the transition from TM oxidation to cation mixing occurs (here  $x_0 = 0.35$  is reached in the subsurface for battery SOC = 50%, which corresponds to bulk  $x = 0.7$  from Figures 2b and 5c);  $\alpha$  denotes the fraction of migrated Ni;  $\beta$  and  $\gamma$  correspond to the amounts of oxidized Ni species participating in the reductions  $Ni^{3+} \rightarrow Ni^{2+}$  and  $Ni^{4+} \rightarrow Ni^{3+}$ , respectively, with  $\alpha = \beta + \gamma$ ; and  $z$  represents the presence of oxygen vacancies near the surface. The compound whose charge balance is described by Equation 2 also fits well with the results in Figure 5b. This accounts for i) a net increase in the  $Ni^{2+}$  population by  $\Delta Ni^{2+} = \alpha + \beta$ , ii) a net decrease in the  $Ni^{4+}$  population by  $\Delta Ni^{4+} = -\gamma$ , and iii) a variation in the  $Ni^{3+}$  population, which depends on the  $\Delta Ni^{3+} = \gamma - \beta$  balance.

We have used a lower maximum cycling voltage compared to other studies (4.2 V versus > 4.5 V)<sup>[12,13]</sup> to avoid deep delithiation of the NMC bulk and thus prevent charge compensation by cation mixing. However, this did not prevent additional Li losses in the region near the cathode surface, leading to the formation of Li-free Ni oxide phases at the surface and an NMC with intermixed Li/Ni cations beyond.

Our study demonstrates that the correlation between battery SOC, determined by the mobilized amount of Li measured by IBA in Figure 2b, and the bulk Ni oxidation state measured by XANES in Figure 5a, can be extrapolated to the subsurface region measured by HAXPES for a common charge compensation mechanism. This condition is valid up to SOC = 50%, as revealed in Figure 5a,b, where TM oxidation is the predominant compensation mechanism. For higher SOCs, where the Li/Ni cation mixing mechanism operates, an estimate of how the Li stoichiometry decreases beyond its transition threshold  $x_0$ ,  $[Li^+] = x_0 - \alpha$ , can be calculated from the relative variation of the populations of oxidized Ni species as  $\alpha = \Delta N^{2+} + \Delta N^{3+} + \Delta N^{4+}$ . In the absence of phase transitions, the appearance of a  $Ni^{2+}$  signal in the HAXPES spectrum can be solely attributed to cation intermixing. In our study, this signal appears in the subsurface region only for samples with SOC > 50%. We rule out irreversible phase transitions based on two observations: i) samples previously charged to full SOC but measured at SOC < 50% show no  $Ni^{2+}$  signal, and ii) capacity fading is minimal (< 0.1% per cycle; see section S7, Supporting Information). Thus, we attribute the  $Ni^{2+}$  signal to reversible  $Ni^{3+/4+}$  migration into Li sites, indicating local cation mixing. Then, the HAXPES data processing allows us to correlate the Ni oxidation state and the remaining Li content for this charge compensation mechanism. Figure 5c compares the evolution of Li concentration ( $x$ ) with increasing SOC in both the NMC811 bulk and the subsurface region (the latter derived from the

interpretation described above). To the best of our knowledge, this is the first study that provides a correlation between Li concentration and the amount of Ni/Li intermixing in the subsurface of Ni-rich NMC cathodes.

Figure 5c reveals that delithiation begins at the cathode surface and progressively extends into the bulk, resulting in an increase in Li content with depth for a given SOC. This explains why the main oxidation state of Ni measured by HAXPES for early SOCs is higher than that obtained by XANES, due to the delayed oxidation of the cathode bulk. Another noticeable effect is that for low SOCs, delithiation rate of the subsurface layer [ $\partial_{SOC}x = -(10 \pm 1) \cdot 10^{-3}$ ] is significantly higher than in the bulk [ $\partial_{SOC}x = -(6.6 \pm 0.4) \cdot 10^{-3}$ ] (as shown by the linear fit of bulk and subsurface points in Figure 5c). This is likely because the kinetics of the redox reaction is limited by Li transport. Consequently, the amount of Li removed from the subsurface layer is not compensated by bulk diffusion. This causes the subsurface layer to exhibit an increasing Li deficiency compared to the cathode bulk (from  $x = 0.85$  at SOC = 0 % to  $x = 0.3$  at SOC = 50 %). Since Li content determines the transition between potential charge compensation mechanisms, it is expected that different mechanisms operate in the bulk, subsurface layer, and surface of the cathode during deep delithiations. Our study reveals that the bulk of the NMC811 cathode maintains charge compensation through Ni oxidation across the entire SOC range (with bulk  $x$  ranging between 1 and 0.35). In contrast, the subsurface layer transitions to charge compensation via Li/Ni cation mixing for SOC > 50% (with subsurface  $x < 0.35$ ), and the surface remains Li-depleted even at low SOCs (with a Ni oxidation state of  $\approx 2.5+$ ), indicating irreversible structural transitions toward cubic phases. Our HAXPES results demonstrate that these phase transitions are confined to the cathode surface inspected by XPS, despite previous studies<sup>[45–47]</sup> suggesting these could propagate tens of nanometers during the initial cycles. Once the Li stoichiometry decreases below the transition threshold  $x_0 < 0.3$ , which occurs here in the subsurface layer but never in the bulk for the used cycling voltage range (2.8–4.2 V), the Li/Ni cation mixing is triggered and the lithiation rate versus SOC drops from  $\partial_{SOC}x = -(10 \pm 1) \cdot 10^{-3}$  to  $\partial_{SOC}x = -(1.8 \pm 0.1) \cdot 10^{-3}$  (as shown by the linear fits in Figure 5c for the subsurface branch). This implies that Li flows mainly from the cathode bulk, decreasing the Li depth profile gradient, which is likely because the involved Ni migration slows down the lithiation kinetics in the subsurface layer.

Figure 6a provides a summary of the Li depth profiles in NMC811 cathodes as a function of the battery SOC, using the depth range where each technique is sensitive. This summary allows us to model the structure induced by the Li depth profiles in NMC particles during battery charge. The model, shown in Figure 6b, delineates three regions: a  $\approx 1$  nm-thick surface shell rich in Li-free cubic phases, a  $\approx 10$  nm-thick subsurface layer deficient in Li compared to the bulk, and the bulk of the particle. As the battery is charged to SOC  $\leq 50\%$ , the subsurface Li deficiency is compensated by an excess in the mean Ni oxidation state (indicating an increase in the  $Ni^{4+}$  population). For higher SOCs (with subsurface  $x < 0.3$ ), the Li deficiency is compensated

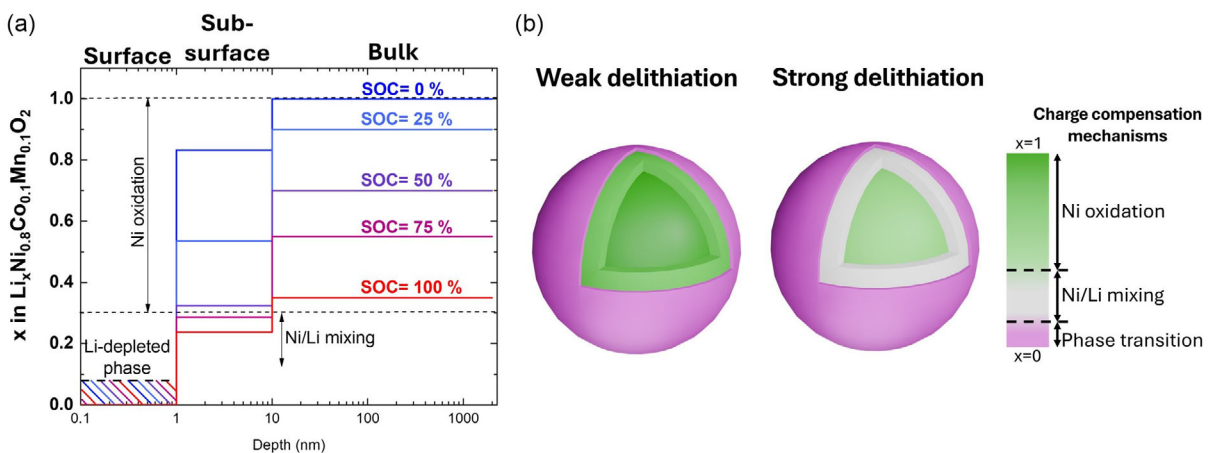


**Figure 6.** a) Changes in estimated Li distribution depth profile along the cathode areas of surface, subsurface, and bulk with increasing SOC. b) Scheme of a NMC particle surface, subsurface, and bulk Li concentration for weak delithiation conditions (SOC = 0%–50%) (left) and strong delithiation conditions (SOC = 50%–100%) (right) indicating the different charge compensation mechanisms operating in each region.

by Ni migration toward Li vacancies. This latter mechanism lowers the mean Ni oxidation state (implying an increase in the  $\text{Ni}^{2+}$  population at the expense of  $\text{Ni}^{4+}$ ) and slows down the delithiation kinetics which homogenizes the Li depth profile.

#### 4. Conclusion

This study presents a comprehensive analysis of the evolution of transition metal oxidation states in NMC811 cathodes, emphasizing the role of various charge compensation mechanisms that influence their electrochemical performance. Since these mechanisms are activated at different Li contents, and NMC secondary particles tend to develop radial gradients in Li concentration, spectroscopy techniques with complementary depth sensitivities are employed. These techniques help correlate the Li depth profile (measured by IBA up to depths of 10  $\mu\text{m}$ ) with the oxidation states of the alloyed transition metals (Ni, Co, and Mn) determined by XPS, HAXPES, and XANES at depths of  $\approx 1$  nm, 10 nm, and 1  $\mu\text{m}$ , respectively, at different battery SOCs. The results indicate that Ni, the major transition metal, is the only one significantly affected by the delithiation process. During moderate Li delithiation ( $\text{SOC} < 50\%$ ), Ni oxidizes from  $\text{Ni}^{3+}$  to  $\text{Ni}^{4+}$  at both bulk and subsurface regions. For deeper delithiation ( $\text{SOC} > 50\%$ ), bulk and subsurface region exhibit different behaviors: Ni continues oxidizing within the bulk, while Ni migrates into Li vacancies at the subsurface region. This difference in behavior is due to the decreasing Li stoichiometry falling below the  $x = 0.3$  threshold at the subsurface region. While the charge compensation by Ni oxidation enables fast and reversible cycling, Ni/Li cation mixing leads to capacity fading and negatively impacts both rate properties and long-term cyclability by hindering Li extraction, which slows down the delithiation kinetics. Quasi-independent of the SOC, the NMC surface remains mostly depleted in Li showing evidence of transformations into electrochemically inactive cubic phases. Overall, these results provide valuable insights into the interplay between transition metal

oxidation, cation mixing, phase transitions, and composition gradients along the NMC811 depth profile. These findings contribute to developing a framework for enhancing the stability and performance of next-generation lithium-ion batteries.

#### Acknowledgements

This work has been supported by the SOLIMEC project funded by the M-ERA.NET Call 2021 and by the Spanish Agencia Estatal de Investigación (PCI2022-132998, PCI2022-132955, and PID2021-124667OB-I00 NanoCatCom project). The authors acknowledge support from the Spanish Ministry of Science, Innovation and Universities through the "María de Maeztu" Programme for Units of Excellence in R&D (CEX2023-001316-M). The authors also acknowledge the support from the Center for Micro-Analysis of Materials (CMAM) - Universidad Autónoma de Madrid for the beamtime with code STD011/23 and its technical staff for their contribution to the operation of the accelerator, and from ReMade@ARI support. The authors are grateful to the SpLine of the European Synchrotron Radiation Facility (ESRF) for the beamtimes with codes A25-2-1048 and A25-2-1072 and to the Instituto de Micro y Nanotecnología IMN-CNM (CSIC).

#### Conflict of Interest

The authors declare no conflict of interest

#### Author Contributions

**Jesus Díaz-Sánchez, Jesús Sánchez-Prieto, and Arturo Galindo** performed the RBS-NRA experiments with the help of **Gastón García**; **Jesus Díaz-Sánchez, Elena Salagre, Juan Rubio-Zuazo, and Celia Polop** performed the XANES and HAXPES experiments; **Jesus Díaz-Sánchez and Elena Salagre** performed the XPS experiments with the help of **Enrique G. Michel**; **Jesus Díaz-Sánchez**

analyzed the RBS-NRA data with the help of Noelia Maldonado, Arturo Galindo, and Gastón García; Jesus Díaz-Sánchez analyzed the XANES, HAXPES, and XPS data with the help of Enrique G. Michel; Ingeborg S. Ellingsen prepared and cycled the NMC cathodes with the help of Daniel Rettenwander; Carmen Morant participated in the SEM measurements; Jesus Díaz-Sánchez and Enrique Vasco developed modeling; Jesus Díaz-Sánchez wrote the manuscript with the help of Enrique Vasco, Enrique G. Michel, and Celia Polop and feedback from all authors; Enrique G. Michel and Celia Polop designed the experiments; Celia Polop coordinated the project.

## Data Availability Statement

The data that support the findings of this study are available from the corresponding author upon reasonable request.

**Keywords:** ion beam analysis · Li-ion battery · NMC cathodes · photoemission spectroscopy

- [1] Y. Ding, Z. P. Cano, A. Yu, J. Lu, Z. Chen, *Electrochim. Energy Rev.* **2019**, 2, 1.
- [2] M. Fichtner, *Batteries & Supercaps* **2022**, 5, e20210024.
- [3] R. V. Moshtev, P. Zlatilova, V. Manev, A. Sato, *J. Power Sources* **1995**, 54, 329.
- [4] J. Morales, C. Perez-Vicente, J. L. Tirado, *Mater. Res. Bull.* **1990**, 25, 623.
- [5] F. Luo, C. Wei, C. Zhang, H. Gao, N. Jiazheng, W. Ma, Z. Peng, Y. Bai, Z. Zhang, *J. Energy Chem.* **2020**, 44, 138.
- [6] K. Y. Chung, K.-B. Kim, *Electrochim. Acta* **2004**, 49, 3327.
- [7] F. Schipper, E. M. Erickson, C. Erk, J.-Y. Shin, F. F. Chesneau, D. Aurbach, *J. Electrochim. Soc.* **2016**, 164, A6220.
- [8] W. Liu, P. Oh, X. Liu, M.-J. Lee, W. Cho, S. Chae, Y. Kim, J. Cho, *Angew. Chem. Int. Ed.* **2015**, 54, 4400.
- [9] A. A. Savina, A. M. Abakumov, *Heliyon* **2023**, 9, 21881.
- [10] S. S. Zhang, *J. Energy Chem.* **2020**, 41, 135.
- [11] R. Jung, M. Metzge, F. Maglia, C. Stinner, H. A. Gasteiger, *J. Energy Chem.* **2017**, 164, 1361.
- [12] F. Lin, I. M. Markus, D. Nordlund, T. Weng, M. D. Asta, H. L. Xin, M. M. Doeff, *Nat. Commun.* **2014**, 5, 3529.
- [13] S.-K. Jung, H. Gwon, J. Hong, K.-Y. Park, D.-H. Seo, H. Kim, J. Hyun, W. Yang, K. Kang, *Adv. Energy Mater.* **2014**, 4, 1300787.
- [14] Q. Zhuang, Y. Su, L. Chen, Y. Lu, L. Bao, T. He, J. Wang, R. Chen, J. Tan, F. Wu, *J. Power Sources* **2018**, 396, 734.
- [15] T. Li, X.-Z. Yuan, L. Zhang, D. Song, K. Shi, C. Bock, *Electrochim. Energy Rev.* **2020**, 3, 43.
- [16] X. Li, A. Gao, Z. Tang, F. Meng, T. Shang, S. Guo, J. Ding, Y. Luo, D. Xiao, X. Wang, D. Su, Q. Zhang, L. Gu, *Adv. Funct. Mater.* **2021**, 31, 2010291.
- [17] A. Gao, X. Li, F. Meng, S. Guo, X. Lu, D. Su, X. Wang, Q. Zhang, L. Gu, *Small Methods* **2021**, 5, 2000730.
- [18] R. W. M. Komalig, G. Shukri, M. K. Agusta, M. H. Mahyuddin, A. Sumboja, A. G. Saputro, R. Maezono, A. Nuruddin, H. K. Diponjono, *Phys. Chem. Chem. Phys.* **2023**, 25, 31374.
- [19] Y. W. Tsai, B. J. Hwang, G. Ceder, H. S. Sheu, D. G. Liu, J. F. Lee, *Chem. Mater.* **2005**, 17, 311.
- [20] Y. W. Tsai, J. F. Lee, D. G. Liu, B. J. Hwang, *J. Mater. Chem.* **2004**, 14, 958.
- [21] A. O. Kondrakov, H. Geßwein, K. Galdina, L. de Biasi, V. Meded, F. O. Elena, G. Schumacher, W. Wenzel, P. Hartmann, T. Brezesinski, J. Janek, *J. Phys. Chem. C* **2017**, 121, 2381.
- [22] W.-S. Yoon, M. Balasubramanian, K. Y. Chung, X.-Q. Yang, J. McBreen, C. P. Grey, D. A. Fischer, *J. Am. Chem. Soc.* **2005**, 127, 17479.
- [23] O. Bondarchuk, A. P. LaGeow, A. Kvasha, T. Thieu, E. Ayerbe, I. Urdampilleta, *Appl. Surf. Sci.* **2021**, 535, 147699.
- [24] G. Shang, Y. Tang, Y. Lai, J. Wu, X. Yang, H. Li, C. Peng, J. Zheng, Z. Zhang, *J. Power Sources* **2019**, 423, 246.
- [25] D. Li, H. Li, D. L. Danilov, L. Gao, X. Chen, Z. Zhang, J. Zhou, R. A. Eichel, Y. Yang, P. H. L. Notten, Degradation mechanisms of C6/LiNi0.5Mn0.3Co0.2O2 Li-ion batteries unraveled by non-destructive and post-mortem methods. **2019**, 416, 163.
- [26] H. Yu, Y. Gao, J. Kirtley, G. Borgmeyer, X. He, X. Liang, *J. Electrochim. Soc.* **2022**, 169, 050520.
- [27] M. J. Ramirez-Peral, J. Diaz-Sánchez, A. Galindo, M. A. Crespillo, C. Morant, C. Polop, E. Vasco, *Energy Storage Mater.* **2024**, 71, 103658.
- [28] A. Machin, M. C. Cotto, F. Marquez, J. Diaz-Sánchez, C. Polop, C. Morant, *Nanomater.* **2024**, 14, 1911.
- [29] R. Gonzalez-Arrabal, M. Panizo-Laiz, K. Fujita, K. Mima, A. Yamazaki, T. Kamiya, Y. Orikasa, Y. Uchimoto, H. Sawada, C. Okuda, Y. Kato, J. M. Perlado, *J. Power Sources* **2015**, 299, 587.
- [30] A. Redondo-Cubero, M. J. G. Borge, N. Gordillo, P. C. Gutierrez, J. Olivares, R. Pérez Casero, M. D. Ynsa, *Eur. Phys. J. Plus* **2021**, 136, 1751.
- [31] M. Mayer, *AIP Con. Proc.* **1999**, 475, 541.
- [32] V. Paneta, A. Kafkarkou, M. Kokkoris, A. Lagoyannis, *Differential Cross-Section Measurements For The 7Li(p,p0)7Li, 7Li(p,p1)7Li, 7Li(p,a0)16O And 19F(p,α,1,2)16O Reactions* **2012**, p. 288.
- [33] J. R. Rubio-Zuazo, G. R. Castro, *Nucl. Instrum. Methods Phys. Res., A* **2005**, 547, 164.
- [34] J. Rubio-Zuazo, M. Escher, M. Merkel, G. R. Castro, *J. Phys.: Conf. Ser.* **2008**, 100.
- [35] J. Rubio-Zuazo, M. Escher, M. Merkel, G. R. Castro, *Rev. Sci. Instrum.* **2010**, 81, 043304.
- [36] B. Ravel, M. Newville, *J. Synchrotron Radiat.* **2005**, 12, 537.
- [37] V. A. Solé, E. Papillon, M. Cotte, P. Walter, J. Susini, *Spectrochim. Acta Part B* **2007**, 62, 63.
- [38] Wavemetrics, *Igor Pro 6.37 Manual* **2015**, Lake Oswego.
- [39] M. Schmid, H.-P. Steinrück, M. Gottfried, *Surf. Interface Anal.* **2014**, 46, 505.
- [40] W. K. Chu, J. W. Mayer y, M. A. Nicolet, *Backscattering Spectroscopy*, Academic Press, New York **1978**.
- [41] K. R. Tallman, G. P. Wheeler, C. J. Kern, E. Stavitski, X. Tonh, K. J. Takeuchi, A. C. Marschilok, D. C. Boc, E. S. Takeuchi, *J. Phys. Chem. C* **2021**, 125, 58.
- [42] Y. F. Nishimura, Y. Kondo, H. Oka, *J. Power Sources Volume* **2020**, 446, 227351.
- [43] O. Karis, S. Svensson, J. Rusz, P. M. Oppeneer, M. Gorgoi, F. Schäfers, W. Braun, W. Eberhardt, N. Martensson, *Phys. Rev. B* **2008**, 78, 233105.
- [44] D. Alders, F. C. Voogt, T. Hibma, G. A. Sawatzky, *Phys. Rev. B* **1996**, 54, 7716.
- [45] N. Y. Kim, T. Yim, J. H. Song, J.-S. Yu, Z. Lee, *J. Power Sources* **2016**, 307, 641.
- [46] S. Zheng, R. Huang, Y. Makimura, Y. Ukyo, C. Fisher, T. Hirayama, Y. Ikuhara, *J. Electrochim. Soci.* **2011**, 4, A357.
- [47] M. C. Biesinger, B. P. Payne, A. P. Grosvenor, Leo W. M. Lau, A. R. Gerson, R. Smart, *Appl. Surf. Sci.* **2011**, 257, 2717.

Manuscript received: March 13, 2025

Revised manuscript received: July 8, 2025

Version of record online: